# Hybridization between plasmonic and photonic modes in laser-induced self-organized quasi-random plasmonic metasurfaces

Van Doan Le, Yaya Lefkir, Nathalie Destouches

# Hybridization between plasmonic and photonic modes in laser-induced self-organized quasi-random plasmonic metasurfaces

*Van Doan Le[1], Yaya Lefkir[1], Nathalie Destouches[1]**

*[1]Univ Lyon, UJM-Saint-Etienne, CNRS, Institut d'Optique Graduate School,*

*Laboratoire Hubert Curien UMR 5516, F-42023 Saint-Etienne, France.*

**Corresponding author: nathalie.destouches@univ-st-etienne.fr*

V. D. Le, Y. Lefkir, N. Destouches,
"Hybridization between plasmonic and photonic modes in laser-induced self-organized quasi-random plasmonic metasurfaces", Nanoscale, 15, 19339 - 19350 (2023),
https://doi.org/10.1039/D3NR05569H

**ABSTRACT**. Plasmonic metasurfaces made of perfectly regular 2D lattices of metallic nanoparticles deposited on surfaces or close to waveguides can exhibit hybridized plasmonic and photonic modes. The latter arise from the excitation of surface or guided modes through the in-plane coherent scattering of periodic arrays. Recently, laser-induced self-organization of random plasmonic metasurfaces has been used to create nanoparticle gratings embedded in protective layers. Despite the broad size distribution and positional disorder of nanoparticles, the resulting nanostructures exhibit strong coupling between plasmonic and photonic modes in transverse electric polarization, leading to dichroism, which is well-reproduced from one laser printing to another. Here, we examine quantitatively the effect of inhomogeneities at the nanoscale on the hybridization between localized plasmonic modes and delocalized guided modes by considering realistic laser-induced self-organized nanoparticle arrays embedded in a two-layer system. By referring to regular samples, we describe the optical mechanisms involved in the hybridization process at characteristic wavelengths, based on far and near field simulations. Two kinds of real samples are considered, featuring different levels of coupling between the plasmonic and photonic modes. The results demonstrate that controlling the statistical properties of plasmonic metasurfaces, such as the nanoparticle size distribution and average position, over areas a few micrometers wide is enough to control in a reproducible manner the hybridization mechanisms and their resulting optical properties. Thus, this study shows that the inherent irregularities of laser-induced self-organized nanostructures are compatible with smart functionalities of nanophotonics, and confirms that laser processing has huge potential for real-world applications.

KEYWORDS: laser induced self-organization, nanophotonics, plasmonic metasurfaces, disorder, hybridization.

**INTRODUCTION**. A regular arrangement of metallic nanoparticles can produce coherent scattered light propagating in-plane and arriving on adjacent nanoparticles in phase with the incident light. The latter may couple to guided modes of a waveguide or generate diffracted orders grazing on the plane of the nanoparticle array. These excited photonic modes may then interact with localized surface plasmon resonance (LSPR) of individual nanoparticles to create hybrid plasmonic photonic states.[1–8] Tailoring this coupling effect enables the design of biosensing materials,[9,10] refractive index sensors,[11] photovoltaic devices[12] or light emitting diodes.[13,14] In addition, the interaction of resonance modes can modify the spectra at visible wavelengths and be used for color applications.[15–21] Many efforts have been devoted to the development of nanofabrication techniques to use these hybrid plasmonic photonic materials in large-scale industrial applications.[11,22–26] Recently, lasers have been employed to produce nanomaterials that support hybrid modes and have demonstrated high performance for a secured color printing technique referred to as printed image multiplexing. Up to four multiplexed images were encoded in a single metasurface for four independent visual observation conditions under white light.[27,28] This ability to encode multiplexed images results from the dichroic properties of the laser-processed samples, which exhibit self-organized silver nanoparticle arrays embedded in a high-index thin film.[29–32] The advantages of using laser-based techniques are their scalability, cost-effectiveness and flexibility. Unfortunately, the resulting nanoparticle arrays normally suffer from intrinsic imperfections from self-organization processes, which include size dispersion and spatial disorder. Despite this randomness at the nanoscale, the optical properties of samples at the macroscopic scale, such as their color in specific observation modes or their dichroism, are

reproducible from one laser printing to another when the processing parameters are maintained constant. Yet, some key questions that are not yet clear and remain unanswered, including the origin of the observed optical properties and the effects of randomness at the nanoscale in these laser-induced systems on the electromagnetic coupling. To advance the development of applications using laser-induced nanomaterials, it is crucial to comprehend the underlying origins of these optical behaviors and assess the tolerance of their optical responses to the intrinsic inhomogeneities of the laser process.

In this paper, we demonstrate the existence of hybrid plasmonic and photonic modes in self-organized quasi-random plasmonic metasurfaces generated by continuous wave laser despite the presence of structural inhomogeneities. The photonic modes propagate in the layered structure as guided modes. Therefore, the hybrid resonance modes can be referred to quasi-guided modes.[1,2,6,11,33] Measured spectra are compared to simulated results where as-fabricatedstructures are considered. A numerical study performed on as-fabricated structures and regular structures, in which array size, spatial disorder and size dispersion are progressively increased, is carried out to estimate their impact on the structure optical response and on the reliability of the simulated results. The comparison with measured results enables quantification of the effects of inhomogeneities in the laser-induced metasurfaces. The article then highlights the different plasmonic and hybrid modes that shape the visible spectra and compare the coupling effect in as-fabricated and regular structures at the near-field scale. Two real samples are investigated, which exhibit different nanoparticle size distributions and support different degrees of coupling, to show that this laser technique can control the coupling strength by simply tuning the processing parameters. The laser-

based method reported here shows that quasi-random nanoparticle array can support intriguing coupling between plasmonic and guided mode resonance, revealing great potential for mass manufacturing of nanomaterials with smart functionalities, which can be applied to anti-counterfeiting or other security purposes.

## RESULTS AND DISCUSSION

**Laser-induced self-organized nanoparticle arrays.** Mesoporous films of amorphous $TiO_2$ containing silver ions and nanoparticles (NP) are processed by a continuous wave (cw) laser slightly focused on the film and moving at a constant speed. Two laser-processed samples are investigated in this article since they exhibit very different nanoparticle size distributions and average nanoparticle grating periods. The first one (Figure 1a) is irradiated at 488 nm wavelength and the second one, investigated later in the article, at 647 nm. Experimental details are given in the Methods section.[29,32] As shown in Fig. 1a, the laser processing induces the growth of silver nanoparticles (white particles) with a broad size distribution (Supplementary Figure S1) along a self-organized periodic structure, whose average period is $\Lambda_x = 300 \pm 40$ nm. Silver nanoparticles are embedded in an intermediate thin film made of a blend of $SiO_2$, from the substrate, and $TiO_2$ from the initial mesoporous film (Figure 1b and Supplementary Figure S2a). The average thickness of this film is $d_2 = 100$ nm. This intermediate layer is covered by a layer containing $TiO_2$, mainly in the form of anatase nanocrystals (Supplementary Figure S2b). The origin of such self-organized nanostructures and the mechanisms leading to this broad size distribution were discussed in some of our previous papers.[29,35–38] The present article focuses on the study of the influence of the array size, size dispersion and spatial disorder at the nanoscale on the optical responses of these laser-

induced self-organized metasurfaces. The present sample exhibits a strong dichroism in extinction (transmission side) with a spectrum showing a single broad peak at 480 nm wavelength for TM polarization (perpendicular to the grating lines) and two peaks at 440 nm and 580 nm for TE

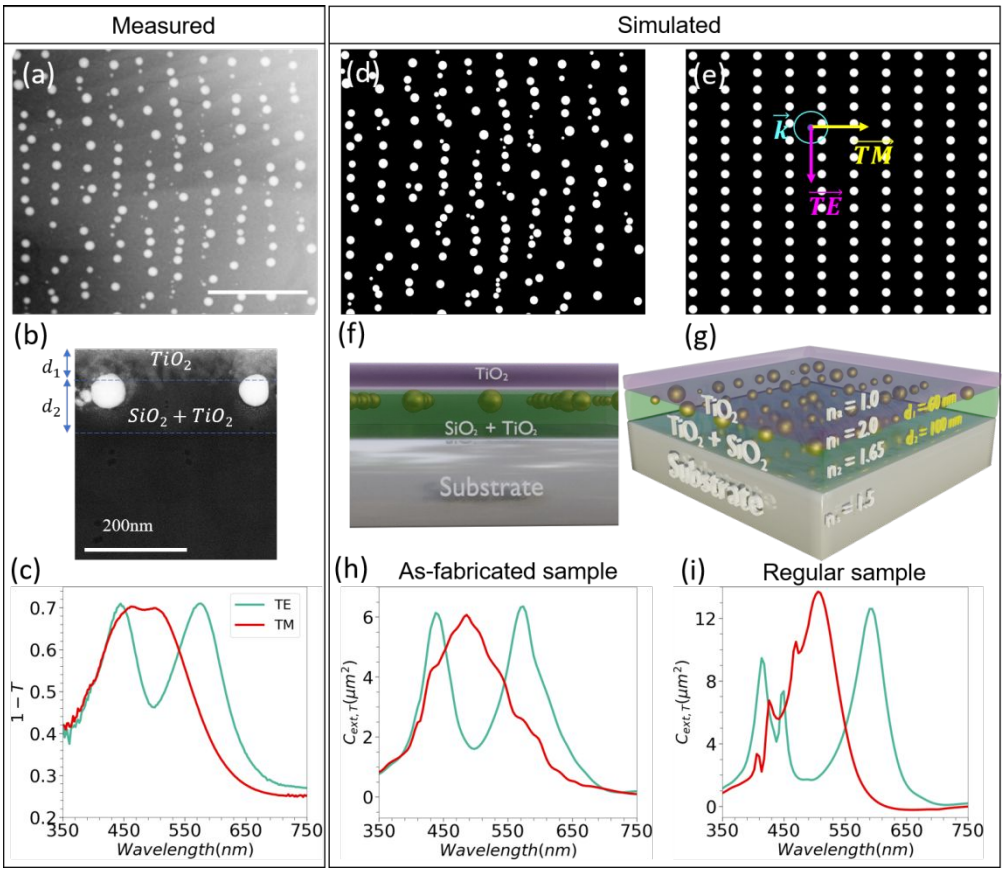


**Figure 1.** (a) Plan-view and (b) cross-section of a Ag NP:$TiO_2$ metasurface induced by cw laser at 488 nm wavelength by scanning transmission electron microscopy. (c) 1 – T of the fabricated sample, where T is the transmission coefficient of the sample measured for TE (electric field parallel to the grating lines) and TM (electric field perpendicular to the grating lines) polarizations under normal incidence. (d) Plan-view, (f) cross-section and (g) 3D view of the as-fabricated sample used in the simulations. All nanoparticles are inside the intermediate layer and tangent to the top layer interface. (e) Plan-view of the regular sample used for comparison with $\Lambda_x$ = 300 nm and $\Lambda_y$ = 180 nm and a nanoparticle diameter equal to 90 nm. The vectors represent the incident wave vector $\vec{k}$ and the two considered polarizations. (h-i) Calculated extinction cross-sections in transmission side of (h) the as-fabricated

sample and (i) the regular one for TE (blue) and TM (red) polarizations. The scale bar in (a) is 1 μm and is the same in (d) and (e).

polarization (Figure 1c). This spectrum can be reproduced at different places on the sample by using the same laser processing parameters. It is therefore independent of the particular ensemble of nanoparticles induced with a certain randomness by the 12.8 μm wide laser beam (diameter at $1/e^2$), and only dependent on statistical properties of the quasi-random nanostructures. In order to investigate the optical properties of the material, we model a realistic sample that reproduces the layer structure and the nanoparticle distribution of the real sample (Figure 1d and Figure 1f-g). The refractive indices of the two layers are optimized to match the simulations with the measured results, while being coherent with the information given by Raman spectroscopy and energy dispersive microscopy (Figure S2). Optimization of the intermediate layer ($n_2$) is provided in Figure S3. Details about the simulations are given in the Methods section. The simulated extinction cross-section spectra of the realistic sample are shown in Figure 1h and are consistent with the measured results of Figure 1c. These results and those of Supplementary Figure S4, where the incidence angle is varied, confirm the choice of the refractive index values in the simulations, which are 1.50 for the glass substrate, 1.65 for the intermediate layer and 2.00 for the top layer (Figure 1g). Silver permittivity is defined by the modified Drude model. A regular structure is then considered to better highlight, later on, the underlying phenomena at the origin of the observed dichroism in the laser-induced samples (Figure 1e). This regular structure has the same parameters as the realistic sample except that the nanoparticle array is periodic, and the nanoparticle diameter is fixed as described in the caption of Figure 1. The spectral variations of the extinction cross-

section of the regular sample exhibit two main dipolar peaks and multiple shoulder peaks (Figure 1i), attributed to the multipolar resonances of metallic particles, as shown in Figure S5. The absence of the shoulder peaks in the spectra of the realistic and fabricated samples is due to the inhomogeneity broadening of resonances. The strong dichroism that occurs, due to the splitting of the dipolar peak for TE polarization, originates from a hybrid plasmonic resonance, as will be further discussed with the near field study. In the next section, we investigate the reliability of the simulated results for varying array sizes at different levels of spatial disorder. Additionally, we aim to analyze how spatial disorder and NP size distribution influence the coupling effects.

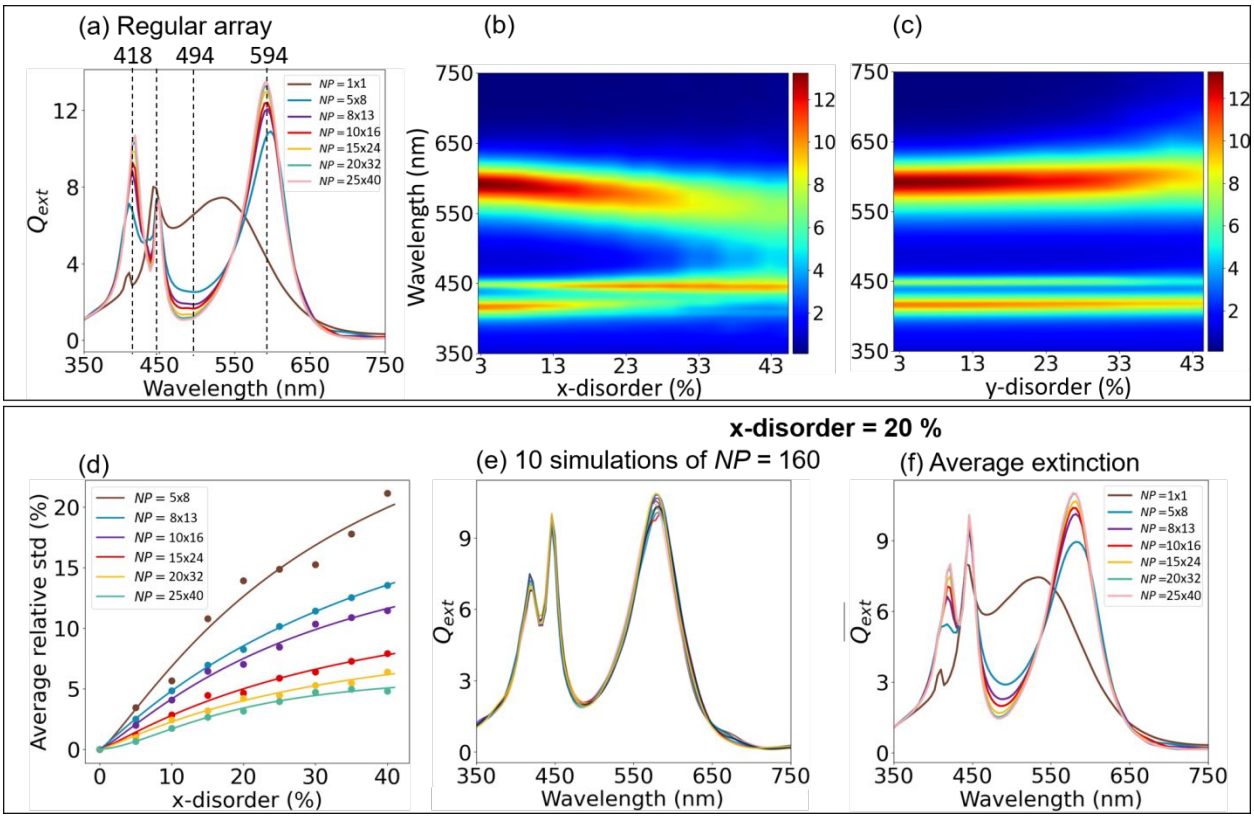


**Figure 2.** (a) Spectral variations of the extinction efficiency $Q_{ext}$ of regular arrays under TE illumination for various numbers of particles. The number of particles in x and y is set to have approximately a square array and the array periods are kept at $\Lambda_x = 300$ nm, $\Lambda_y = 180$ nm. The particle diameter is 90 nm. (b-c) Extinction efficiency $Q_{ext}$ for arrays of 640 NPs (described in Supplementary Figure S5) where the positional disorder increases along the x- and y-axis respectively. (d) Relative average standard deviation with which the average extinction efficiency $\overline{Q_{ext}}$ (defined in the Methods section, and calculated over 10 spectra) is given for each array size as a function of the degree of x-disorder. (e) Extinction efficiency $Q_{ext}$ of ten different simulated arrays with NP = 160 and x-disorder = 20%. (f) Average extinction efficiency $\overline{Q_{ext}}$ at x-disorder = 20%.

**Effect of the array size, NP size dispersion and NP spatial disorder on collective resonances.** Unlike other techniques where each individual nanostructure is well-defined, laser processing modified simultaneously several parameters, resulting in the formation of random metasurfaces with different structural inhomogeneities, including difference in particle size and organization. Laser

processing can lead to varying levels of non-uniformity across the samples. Therefore, the samples are characterized by their statistical properties. Despite these inherent inhomogeneities, the optical responses of the samples are well-reproduced when a specific laser parameter is applied. The first question here arises when doing electromagnetic simulations of NP assemblies is to know how many NPs should be considered to provide reliable simulated results that accurately represent the statistical properties of real sample measured over a large area. To address this question, we first quantify the impact of spatially disorder and size distribution on the optical responses. . Figure 2a shows the extinction efficiency $Q_{ext,T}$ of regular matrices for different numbers of NPs per array. $Q_{ext,T} = \frac{C_{ext,T}}{N_p * \pi R^2}$, where $C_{ext,T}$ is the extinction cross-section in transmission side, $N_p$ is the number of the particles in the array and R is the particle radius. It allows to better compare the results obtained for different numbers of NPs. When increasing the number of particles in the regular array, the peaks at 418 nm and 594 nm become more pronounced as well as the dip at 494 nm, evidencing the collective behaviors of the NPs array at these wavelengths. On the other hand, the peak at 447 nm, which is attributed to the quadrupolar resonance, remains insensitive to the array size. In addition, the optical response starts to reach the saturation at array of NP = 20 x 32. Therefore, in the next simulations introducing spatial disorder and size distribution (Figure 2b, c & Figure S7), the particle number is set to 20 x 32.

Spatial disorder is introduced by a random displacement of each nanoparticle along the x or y axis (Supplementary Figure S6). An increase in the spatial disorder corresponds to a wider standard deviation of the displacement histograms in x or y. Simulations (Figure 2b) show that when the x-disorder increases, the extinction efficiency at 418 nm and 594 nm attenuate and shift toward the

position of the dip at 494 nm whose amplitude decreases too. At high level of disorder, the peaks and dip start to merge together and the extinction spectrum tends more and more to the one of a single nanoparticle. The long wavelength peak is characteristic of a hybrid plasmonic resonance and corresponds to a strong enhancement of the absorption by the LSPR at a wavelength where constructive interferences occur between the waves scattered by each period in the sample plane. These constructive interferences are due to fact that the field scattered by the NPs arrives in phase with the incident field on the adjacent NPs.[3] The higher the disorder, the more random is the phase difference between the scattered fields by the rest of the array and the incident field on each NP, which reduces the collective effect on the absorption enhancement. Conversely, the relative amplitude of the quadrupolar resonance (at 450 nm) slightly increases to reach the one of a single particle. In contrast to x-disorder, increasing the disorder along the y-axis does not change the positions of the peaks and dip (Figure 2c). The peaks extinction at 418 nm and 594 nm is slightly decreased, and the dip at 494 nm remains visible regardless of the y-disorder. This behavior is very similar to one observed in Figure S7a, where various size distributions centered on an average size of 60 nm are considered. Because of the smaller particle sizes, the quadrupolar mode is absent, and the width of the resonance peak is narrower linked to the decreased radiation damping of the resonance.[39,40] The results from Figure 2b, c and Figure S7a demonstrate that the regularity along the x-axis is the most crucial parameter that govern the coupling behavior when compared to the others. Therefore, in the following investigations, we will vary particles along the x-axis while keeping particle size (D = 90 nm) and y-disorder = 0 %.

When disorder increases, the results start depending on the particular arrangement of NPs considered in an array. The higher the array size, the more reproducible is the simulated spectrum for different arrangements with the same degree of disorder. To limit the calculation time, we limit the NP number per array to 1000 (25 x 40) and we average over 10 different arrangements. Figure 2d gives an estimate of the error with which the average spectra for a given x-disorder is calculated when considering various NP numbers per array. This error is calculated by using the relative average standard deviation of the calculated spectra. Ten simulations with different spatial distributions are carried out for each disorder value and array size (see Methods for the detail equations). As shown in the figure, to maintain reliable simulated results when the disorder increases, higher numbers of NPs must be considered in the arrays. Figure 2e show 10 spectra calculated with different arrangements and the same degree of disorder (20 %) and NP number (10 x 16), which corresponds to an average relative error of 7 %. Figures S8 and S9 provide further simulations about the spectral variation as a function of disorder and array size, respectively. Figure 2f, which can be compared to Figure 2a, shows the average spectra simulated for 20 % of x-disorder and an increasing number of NPs. The spectra converge from 20 x 32 NPs and the difference between 10 x 16 NPs and 20 x 32 NPs corresponds only to an average relative error of 4.5%.

Turning to the question of whether the array size and spatial disorder of as-fabricated sample in Figure 1d are precise enough to provide reliable optical response of the real sample, we first quantify the disorder degree of the as-fabricated sample. As shown in Figure S10, by comparing the histogram and plan-view of a generated array, the disorder level of as-fabricated sample is

determined as being ~20% along the x and y axes. In addition, the array size is equivalent to an array of 10 x 16 NPs, which corresponds to a relative average error of 7 %. In conclusion, the statistical optical properties of real samples, which is measured over an area of 2 by 2 $mm^2$, can

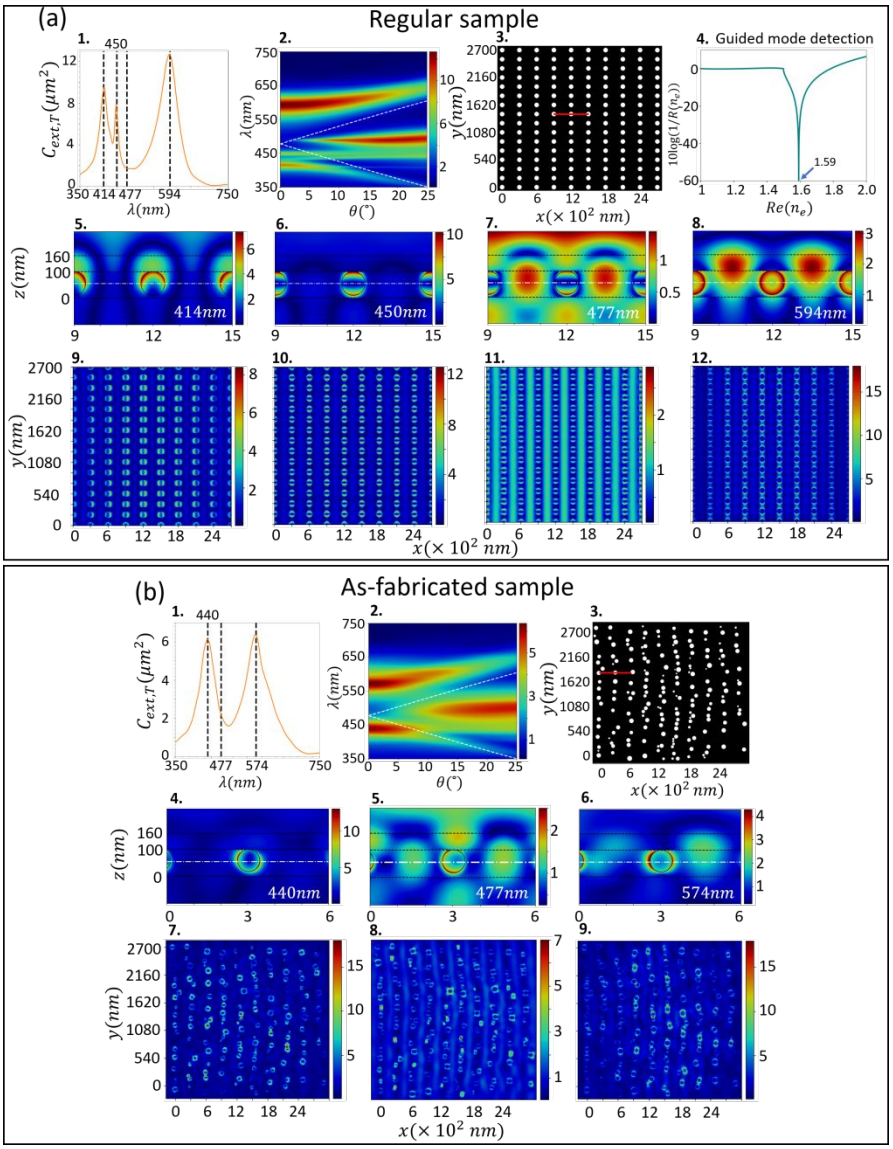


**Figure 3.** Spectral variations of $C_{ext,T}$ under normal incidence for (a.1) the regular and (b.1) as-fabricated sample. The vertical dotted lines indicate the wavelengths at which the near field is calculated below. Spectral and angular maps of $C_{ext,T}$ for (a.2) the regular and (b.2) as-fabricated sample, with incident plane parallel to the xz-plane. The white dashed lines indicate the guided modes excited by $\pm 1$ diffraction orders. Plan-view of the (a.3) regular and

(b.3) as-fabricated NP arrays. (a.4) Pole of the reflection coefficient R of the two-layer system without nanoparticles. (a.5-12, b.4-9) cross-section and plan-view of the near field intensity distribution at selected wavelengths (shown in fig. a.1 and b.1 respectively). The nearfield intensities shown in plan-view are calculated on the white dashed dotted lines drawn in the cross-section pictures. The nearfield intensities shown in cross-section are calculated on the red lines in figure a.3 and b.3. The black dashed lines indicate the layer interfaces. All calculations are implemented for TE polarization.

be well-reproduced by a few micrometers wide as-fabricated sample and the collective effects are still largely present in the laser-induced self-organized metasurfaces despite the intrinsic inhomogeneities. In the next section, we will investigate the underlying mechanisms of these collective behaviors using simulations from as-fabricated sample, which only arise for TE polarization.

**Coupling between plasmonic and photonic resonances.** To undoubtedly highlight the optical mechanisms that occur at characteristic wavelengths, we compare further the optical properties of the as-fabricated sample (Figure 3b.3) under TE polarization with the ones of the regular sample (Figure 3a.3). As already described in Figure 1, their extinction cross-section spectra (Figure 3a.1 and Figure 3b.1) exhibit a similar split of the dipolar plasmon mode, characterized by two peaks and a dip, which are identified by vertical dotted lines in Figure 3a.1 and Figure 3b.1. In addition, the peak at 450 nm in Figure 3a.1 of the regular sample can be attributed to the quadrupolar resonance. This resonance exhibits field enhancement with four maxima distributed on the particle surface:[41] two in cross-section (as illustrated in Figure 3a.6) and two in plan-view (as shown in

Figure 3a.10). To confirm the quadrupolar nature of the peak at 450 nm, we decompose the total extinction in transmission side in Figure 3a.1 into the contribution of each resonance mode. As shown in Figure S5c, the dipolar mode features two peaks at 414 nm and 594 nm, resulting from the coupling. In contrast, the peak of quadrupolar mode arise distinctly at 450 nm, separate from the peaks originating from dipolar mode. Consequently, the peaks in the total extinction spectrum (Figure 3a.1) appear separately. Conversely, the decomposition of the realistic sample reveals the overlap of the first peak of the dipolar mode and the quadrupolar mode at 440 nm, contributing to the enhancement of the first peak in the total extinction spectrum (Figure 3b.1).

On the regular sample, the dip at around 477 nm results from the interference between the incident wave and guided modes of the double layer structure excited through diffraction by the nanoparticle grating. This interference creates a standing wave pattern, where nanoparticles reside at the nodes, *i.e.* the positions of minimum intensity (Figure 3a.7&11). Similar observations were already reported many times[2,42] and can be explained by the $\pi$ phase shift of the scattered field at the nanoparticle surface compared to the incident wave.[5] Correspondingly, the field enhancement and absorption at the nanoparticle surface are almost null and the material is almost transparent at this wavelength. As demonstrated by Amra et al.,[43] the effective refractive index of guided modes that can propagate in a multilayer structure corresponds to the complex poles of the reflection coefficient of the structure. Figure 3a.4 shows the reverse reflection coefficient of the two-layer structure as a function of the effective refractive index. As we know that the field is negligible on nanoparticles at the considered wavelength, we assume in this simulation that the intermediate layer is nanoparticle free. The results show that one guided mode can propagate in the structure,

and lead to an effective index $n_e$= 1.59. Assuming that this guided mode is excited through the first diffraction order of the 300 nm period grating of nanoparticles, one can deduce the wavelength at which the excitation should occur: $\lambda = \Lambda\, n_e = 300 \text{ x } 1.59 = 477$ (nm). This value points out the beginning of the plateau where $C_{ext,T}$ is minimum on Figure 3a.1, and is then compatible with the rigorous calculation of the scattered field. Comparing now the near field distribution of the as-fabricated-structure with the one of the regular sample at the position of the calculated guided mode (477 nm), the similarities are striking despite the heterogeneities of the as-fabricated structure (Figure 3b.5& 8). One can thus conclude that the dip in the $C_{ext,T}$ spectrum of the as-fabricated structure also results from the excitation of a guided mode in the structure, whose effective index is considered to be also equal to 1.59 in the following discussion. It is essential to highlight that the coupling between the diffraction order from a nanoparticle array and a guided mode is most favorable when there is a supporting waveguide layer. Conversely, when the nanoparticle array is embedded in a homogeneous medium, the diffraction order can propagate in the plane of the array, leading to the emergence of surface lattice resonance.[3] This phenomenon is depicted in Figure S11, where surface lattice resonance occurs in TE polarization of the as-fabricated nanoparticle array embedded in a homogeneous medium with n = 1.65, resulting in enhanced extinction at around 590 nm.

Actually, two guided modes can propagate in the structure, one going to the right, the other to the left. Under normal incidence, the wavelength at which these two modes are excited is the same. But under oblique incidence, according to the grating equation (Equation 1), the left (or backward) and right (or forward) modes are excited by two different wavelengths $\lambda_{\pm}$.

$$\lambda_{\pm} = \Lambda \frac{n_e - n_i sin\theta_i}{\pm m} \quad , \tag{1}$$

where $\theta_i = 0°$ is the incident angle, $n_i$ is the refractive index of the incident medium, $\pm m$ is the order of diffraction ( $\pm 1$ in the present case), Λ is the grating period and incident plane is parallel to the xz-plane. Assuming that $n_e$= 1.59, $\lambda_{\pm}$ are plotted with white dashed lines in Figure 3a.2 and Figure 3b.2 that display the spectral and angular dispersion of the extinction cross-section in transmission for both samples. At small incidence angle, when the guided modes spectrally overlap with the dipolar mode of the LSPRs of individual nanoparticles, their interaction turns into a dip in the extinction. When the photonic modes move outward from this spectral area for larger angles, the white dotted lines get closer to the extinction peaks. In addition, the dipolar mode of individual nanoparticles starts to reinforce at around 494 nm. This behavior was also observed in other periodic structures, with two-dimensional gold nanoparticles[5] or one-dimensional gold grating[1] placed on top of an ITO waveguide. Here, we report this behavior for a structure with spatial disorder and size-inhomogeneity, namely the laser-induced self-organized structure (Figure 3b.2). The latter exhibits a very similar behavior with broader resonances due to the heterogeneous broadening. Interestingly, the quadrupolar mode of the LSPR emerges on the spectrum of the as-fabricated structure when dipolar contribution is attenuated by its interaction with a guided mode, *i.e.* in the angular range [10°;12°]. The quadrupolar resonance mode does not contribute to the excitation of the guided modes and appears as a horizontal stripe insensitive to the incident angle. For TM polarization (Supplementary Figure S12a.2 and Figure S12b.2), the angular behavior of $C_{ext,T}$ features LSPRs whose resonance wavelength is almost independent of the incident angle. The optical characteristics of the sample exhibit different responses when the incident angle varies

in the yz-plane, as depicted in Figure S13. Unlike what is observed in Figure 3a.2 and 3b.2, changing the incident angle does not result in the splitting of the extinction peaks. When the polarization is oriented parallel to the incident plane, an increase in the incident angle leads to a reduction in the coupling strength, manifesting as slight shift and decrease in the extinction peaks. This effect occurs because the in-plane component of the incident field (Ey) decreases as the incident angle increases, thereby reducing the diffraction efficiency of the diffraction order from the array.

The coupling between the photonic and plasmonic modes leads to the generation of hybridized states, which manifest themselves as extinction peaks, featuring the characteristics of both modes. For the peak at $\lambda = 414$ nm, the electric field is mainly enhanced and localized around the metallic particle with a small field enhancement on top of the particles, indicating the dominance of LSPRs (Figure 3a.5 and Figure 3a.9). On the other hand, in Figure 3a.8, the field distribution at 594 nm shows stronger feature of photonic nature, where not only does the field distribute around the metallic particles, but it also concentrates in the top layer between the nanoparticles. This is an indication of the coexistence of plasmonic and photonic modes, which can be referred to waveguide-plasmon polariton.[1,2,42] In addition, as shown in Figure 3a.12, the emergence of the hybrid state causes the electric field redistribution with enhancement between the nanoparticles, evidencing a strong coupling between particles. The comparison of the near field distribution at the two extinction peaks for the as-fabricated sample (Figure 3b.4, Figure 3b.6, Figure 3b.7 and Figure 3b.9) show, as on the regular sample, a field located on the nanoparticles at the lower wavelength and located both on the nanoparticles and in the top layer at the higher wavelength.

The spatial disorder and size dispersion significantly alter the field intensity from one nanoparticle to another. However, the comparison with the regular structure confirms that mode hybridization takes place in the as-fabricated structure. Additional nearfield plan-views calculated at the middle of the $TiO_2$ layer are given in Figure S14. The corresponding simulations of Figure 3 for TM polarization are shown in Figure S12, and evidence that only LSPRs in the whole wavelength range are observed.

Figure 4a-e further investigates the near field intensity distribution when the regular structure is illuminated by a plane wave under $\theta_i = 10°$. The dip at 477 nm under normal incidence, where the scattered field is π-out of phase with the incident wave on the nanoparticles, has been split in two dips, which can be determined using equation (1), at 425 nm and 529 nm (Figure 4a). The shorter wavelength corresponds to the forward mode, while the longer wavelength corresponds to the backward mode. When interfering with the incident light within the structure, the forward mode leads to an interference pattern that is tilted to the left on the cross-section view, as simulated in Figure 4c (cross-section) and as can be deduced from the wave vectors direction of the two interfering waves. As the simulated structure is finite and illuminated with a plane wave, the excitation of the forward mode also leads to an accumulation of light intensity to the right (plan-views at z = 55 nm and z = 130 nm in Figure 4c). It should be noticed that the quadrupolar mode

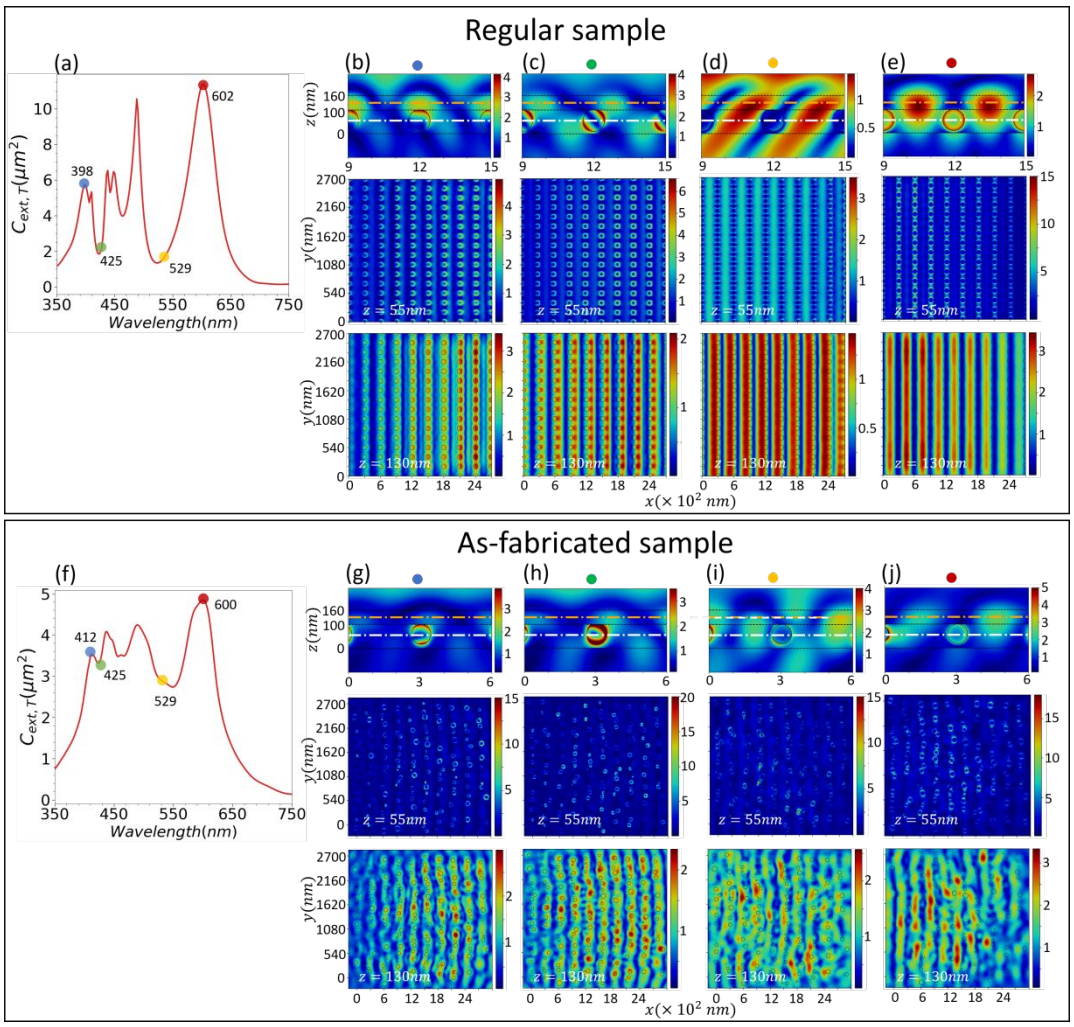


**Figure 4.** Optical properties of the regular and as-fabricated structures under an oblique incidence angle of 10˚. (a, f) Extinction cross-section spectrum of both structures. (b-e, g-j) Near field intensity on the cross-sections and plan-views at characteristic wavelengths. The forward (green dot) and backward (yellow dot) guided modes excited π-out-of-phase with the incident wave at the nanoparticle surface show light that propagates and accumulates to the right and left, respectively. The blue and red dots correspond to the hybridization of the forward and backward mode, respectively, with the dipolar plasmon mode of individual nanoparticles. The cross-sections are calculated at the same position as the one shown in Figure 3 (red line). The white (z = 55 nm) and orange (z = 130 nm) dashed dotted lines indicate where the near fields on the plan-view are calculated. The black dashed lines represent the layer interfaces. Black circles in plan-views (z = 130 nm) represent the positions and sizes of NPs.

occurring at 440 nm, which does not excite the guided mode itself, partly overlaps with the interference pattern associated to the forward mode at 425 nm wavelength (Figure 4c). At shorter wavelength, the hybridized mode features an extinction peak at 398 nm where the field enhancement at the particles top surface and the field accumulation at the right of the plan-views can be observed (Figure 4b). The backward mode excited at 529 nm leads to an interference pattern tilted to the right on the cross-section views and to an accumulation of light to the left on the plan-views at z = 55 nm and z = 130 nm (Figure 4d). The resulting hybridized mode occurs at 602 nm (Figure 4e) and leads to an enhanced absorption of the dipolar plasmon mode and a field enhancement in the upper layer that accumulates to the left. While less regular, these features are also observed on the as-fabricated structure whose simulations are gathered in Figure 4g-j. Consequently, the size dispersion and spatial disorder of nanoparticles resulting from laser processing do not significantly prevent the occurrence of the hybridized states between plasmonic and photonic modes for TE polarization.

This laser technique not only produces metamaterials that sustain hybrid modes but it can also control the coupling strength through the spectral overlapping between the resonance modes and diffraction efficiency of the nanoparticle grating. The spectral overlapping can be changed by varying the waveguide thickness, particle size, or the grating period of the self-organized nanoparticle array. Specifically, altering waveguide thickness result in different coupling strengths.[33] A thin waveguide with weak confinement of guided mode, yields weaker coupling, while increasing the waveguide thickness enhances electric guided field. However, an excessively thick waveguide may shift the intensity of the excited guided mode away from the LSPR of NPs,

resulting in weaker coupling (Figure S15). The optimal thickness corresponds to the maximum field, aligning with the point where spectral overlapping is strongest and where the wavelength of the excited guided mode arises in the middle of the LSPR as shown in Figure 1 and Figure 3. Nonetheless, in our fabrication approach, a more straightforward way to control the coupling strength is to adjust the grating period through laser wavelength, which will be discussed further in the subsequent sections. As explained in our previous article[29] this grating period is proportional to the incident laser wavelength used for processing.

The laser wavelength and other parameters as the laser power or scan speed can also affect the average nanoparticle size and their size dispersion, and in turn the diffraction efficiency of the nanoparticle array. Figure 5 shows the results related to another real sample, which was produced at $\lambda = 647$ nm, with a power of 500 mW and a scan speed of 300 µm/s, and the corresponding simulations of the realistic structure. The longer laser processing wavelength leads to a larger average grating period of 400 nm (Figure 5a). Assuming the thicknesses shown in Figure 5d, deduced from SEM picture of the sample cross-section (Figure S16a), the same refractive indices as previously and a film free of nanoparticles, one can use the same approach as previously to determine the occurrence of one guided mode in the structure with an effective index of 1.56 (Figure 5b). Multiplying this value by the average grating period, one can find that under normal incidence, the guided mode can be excited at 624 nm, which matches well the position of the blue-edge of the second dip in transmission in Figure 5c and Figure 5f. At this wavelength, the near

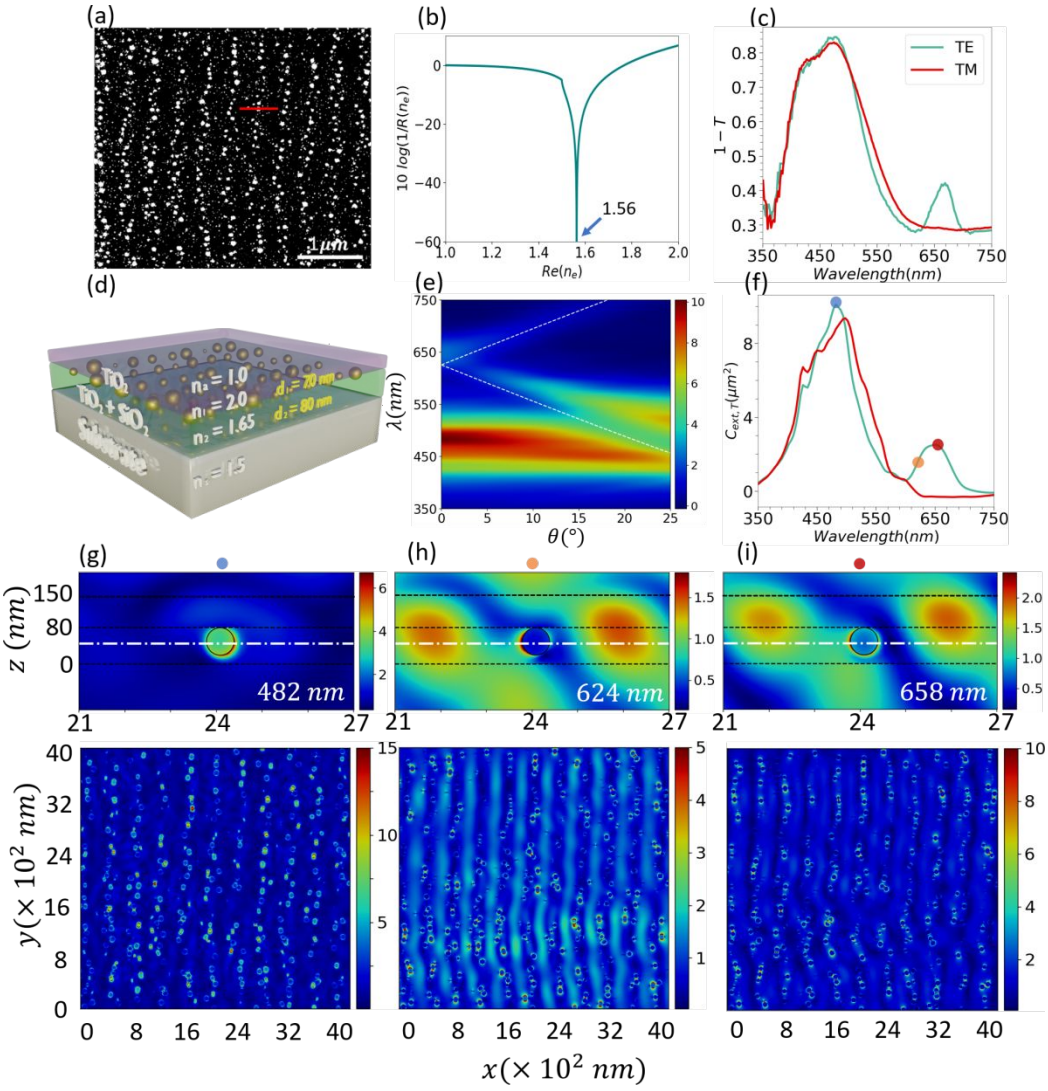


Figure 5. (a) Plan-view of the as-fabricated sample simulated from a real sample laser processed at λ = 647 nm, with power of 500 mW and scan speed of 300 μm/s. (b) Reverse reflection coefficient R of the two-layer system without nanoparticles in logarithmic scale. 1.56 is the effective index value of the guided mode considered to draw the dash lines in (e). (c, f) Extinction in transmission of the fabricated and simulated sample, respectively. (d) 3D sketch of the simulated structure. (e) Spectral variations of the extinction cross-section in transmission of the as-fabricated sample. (g-i) Near field intensity on the cross-sections and plan-views at the characteristic wavelengths.

field distribution shows interference patterns with low excitation on the particle surface (Figure 5h). As the experimental size distribution (shown in fig. S12b) shows smaller sizes than in the first

sample, the dipolar mode of the LSPRs (first peak in Figure 5c) is blue-shifted compared to the first sample, resulting in strong electric field enhancement at 482 nm confined around nanoparticles, as shown in Figure 5g. Conversely, the hybrid mode excited at higher wavelength (658 nm) with the electric field is delocalized and mainly distributed around surrounding media. Consequently, the resonance of the plasmonic and photonic modes do not spectrally overlap, which results in weak coupling effect. Note that in this weak coupling regime, the excited guided mode is tuned out of the LSPRs, appearing closer to the extinction peak compared to the first sample. Therefore, it features similar near field pattern to the peak (Figure 5h & i). Simulating the spectral and angular variations of the extinction cross-section in transmission (Figure 5e), shows that the spectral overlapping occurs for incidence angles above 15°. Then, the coupling between the photonic and plasmonic modes leads to a reduced absorption followed, at longer wavelength, by an absorption enhancement. The inhomogeneity of this other laser-induced quasi-random plasmonic metasurface does not prevent the excitation of guided modes and the occurrence of hybridization. These examples, selected among a large database of laser-processed samples produced by tuning the laser wavelength, power, scan speed and laser focus, are two extreme cases where dichroic properties are observed. They should be representative of a large number of laser-processed samples in which self-organized periodic patterns occur.

## CONCLUSIONS

In conclusion, this study investigates the effect of intrinsic spatial disorder and size dispersion that exist in the laser-induced self-organized plasmonic metasurfaces on their optical properties. Simulations are carried out on regular structures in which different array sizes, levels of disorder

and NP size distributions are introduced, and on realistic structures elaborated from three dimensional reconstructions of real samples. The degree of disorder along the y direction does not appear as an influent parameter while the one long the x direction is shown to affect the collective effect and the mode hybridization. The disorder of the laser-induced samples is estimated at a relatively low level of 20 %. By proving the adequacy of the as-fabricated sample in reproducing the statistical properties of experimental sample and further investigating the near field distribution, we quantitatively characterize the coupling between the dipolar mode of the LSPR of individual metallic nanoparticles and guided modes excited through diffraction by the nanoparticle array in the layered structure. The near and far field investigations demonstrate that the inhomogeneities inherent to the fabrication technique, while striking when looking at the structures at the nanoscale, do not disturb so much the overall interaction with light. Two representative kinds of laser-induced nanostructures, exhibiting different periods, size distributions and dichroism, confirm this conclusion. Laser processing appears then as a powerful technology to produce useful functional metamaterials despite intrinsic imperfections. With its simplicity, cost-effectiveness and scalability, it is very promising for industrial applications, which exploit the fascinating optical properties of plasmonic materials.

## METHODS

**Film Elaboration**. Experiments are carried out on mesoporous films of amorphous $TiO_2$ impregnated with silver salt and deposited on glass slides whose elaboration has been described in previous articles already.[24, 25] The films are elaborated by sol-gel process where the sol contains titanium tetraisopropoxide (TTIP, Aldrich; 97%), acetylacetone (AcAc, Aldrich; 99%)

hydrochloric acid (HCl, Roth; 37%), ethanol (EtOH, Carlo Erba; absolute), Pluronic P123 ( $(PEO)_{20}$) $(PPO)_{70}(PEO)_{20}$, Aldrich; MW: 5000), and deionized water ($H_2O$) with the molar ratios: TTIP/P123/ethanol/HCl/$H_2O$/AcAc = 1:0.025:28.5:0.015:29.97:0.5. The films are annealed at $340^{\circ}$ to form mesoporous titania films. The latter are soaked in an aqueous ammoniacal silver nitrate solution for 30 min to generate silver ions and then exposed to UV light (400 μW.cm $^{-2}$ at 254 nm).

**Laser Processing**. An Ar-Kr CW laser is used to generate the self-organized nanoparticle structures. The experiment is carried out at two different wavelengths, 488 nm and 647 nm. The laser beam is slightly focus under normal incidence on the sample surface by a 10x microscope objective (Olympus MPlan N, N.A 0.25), where it has a beam diameter of 12.8 μm. The samples are placed on a translation stage and moved at constant speeds. At 488 nm wavelength, the power is 250 mW and the scan speed 300 μm/s. At 647 nm, the power is 500 mW and the scan speed 300 μ m/s.

**Spectral Characterizations**. Transmission spectra were measured with a Cary 5000 spectrophotometer from Agilent Technologies.

**Average Standard Deviation**. The standard deviation at each wavelength ($\lambda$) reads:

$$\sigma_\lambda = \sqrt{\frac{1}{N}\sum_{i=1}^{N=10}(Q_{i,\lambda} - \mu_\lambda)}$$

with $N = 10$ the number of simulations, $Q_{i,\lambda}$ the extinction efficiency at wavelength $\lambda$ of the simulation number $i$ and $\mu_\lambda = \frac{1}{N}\sum_{i=1}^{N=10} Q_{i,\lambda}$ is the average extinction efficiency at wavelength $\lambda$. The average relative standard deviation is then

$$\sigma = \frac{1}{N_\lambda}\sum_{\lambda=350}^{750}\frac{\sigma_\lambda}{\mu_\lambda}$$

with $N_\lambda$ is the number of wavelength values.

**Introduction of disorder**. The disorder levels are introduced using Gaussian distribution

$$f(v) = \frac{1}{\sigma\sqrt{2\pi}} e^{-\frac{1}{2}\left(\frac{v-\mu}{\sigma}\right)^2}$$

with μ is the mean of the distribution, $\sigma$ is the standard deviation.

Regarding x-disorder, we set μ to 0, and for σ, we varied it in the range of 0 to 150 nm, which corresponds to values from 0 to 100%. It's worth noting that the upper limit of 150 nm is equivalent to half of $\Lambda_x$. For y-disorder, we also maintained μ at 0, while σ ranged from 0 to 90 nm, covering the disorder level from 0 to 100%. Here, the upper limit of 90 nm mirrors half of $\Lambda_y$. When it comes to size disorder, we chose a μ value of 60, and σ was adjusted in the range of 0 to 60 nm, corresponding to the level from 0 to 100%.

**Electromagnetic Modeling**. *Spectra and Nearfield Simulations*. All the simulations were carried out with *Smuthi*,[44] a python package for simulating the electromagnetic scattering by multiple particles near or between planar interfaces. The method combines the T-matrix method to calculate multiple scattering from the particle assembly and the scattering matrix formalism to take into

account the layer system.[45,46] Once the scattered field coefficients of the particles are computed, all quantities of interest can be derived in a post-processing step such as the electric near field or cross-sections. In the context of particles located near planar interfaces, the extinction cross-sections are derived from the optical theorem in which two extinction cross-sections are calculated. The first one accounts for the reflection side and the other one for the transmission side. Consequently, the extinction cross-sections for transmission, $C_{ext,T}$, and reflection $C_{ext,R}$ are calculated as the ratio of the time-average power lost in transmitted or reflected direction, $\langle P_{ext,T} \rangle$ or $\langle P_{ext,R} \rangle$, respectively, and the intensity $I_0$ of the incident plane wave as $C_{ext,T} = -\langle P_{ext,T} \rangle / I_0$, and $C_{ext,R} = -\langle P_{ext,R} \rangle / I_0$, respectively.[46] Silver permittivity is defined by the modified Drude model:

$$\epsilon(\omega) = \epsilon_{\text{ib}} - \frac{\omega_p^2 \epsilon_0}{\omega^2 + j\omega\Gamma}$$

where $\epsilon_{\text{ib}} = 3.7\ \epsilon_0$ is the contribution of interband transition and $\epsilon_0$ the vacuum permittivity, $\omega_{\text{p}}$ is the plasma frequency with $\hbar\omega_p = 8.89\ eV$, $\Gamma = \Gamma_0 + Av_F/r$ is the damping constant with $\Gamma_0 = 17.6\ meV$ the damping constant of bulk silver, $A = 1$ a constant, $v_f = 1.39\ x\ 10^6\ m/s$ the Fermi velocity and $r$ the particle radius.

*Guided Mode Calculation*. The calculation is carried out using the method proposed by C. Amra *et al.* [43] A two-layer system, similar to the one shown in figure 1 or figure 5d, but without nanoparticles is considered. $n_0$, $n_1$, $n_2$, $n_s$ are the refractive indices of the superstrate, $TiO_2$ layer, intermediate layer and substrate. $e_1$ and $e_2$ are the thicknesses of the two layers respectively. As

demonstrated by Amra et al., the poles of the complex reflection coefficient correspond to guided modes of the structure. The complex reflection coefficient is defined as: $r_0 = \frac{\tilde{n}_0 - Y_0}{\tilde{n}_0 + Y_0}$

Where $\tilde{n}_0 = \begin{cases} \frac{1}{\eta_0 \mu_{r_0}} n_0 cos\theta_0 \ (TE) \\ \frac{1}{\eta_0 \mu_{r_0}} n_0 / cos\theta_0 \ (TM) \end{cases}$ is the effective refractive index of the superstrate, $\theta_0$ is the incidence angle, $\eta_0$ is the impedance of vacuum, $\mu_{r_0}$ is the superstrate relative permeability and $Y_0$ is the complex admittance at the first interface of the multilayer, which is defined as the ratio of tangential components of the electric and magnetic fields. For a multilayer system the complex admittance can be seen as the effective refractive index in a homogeneous medium. To calculate $Y_0$ , we can apply the recursive relation:

$$Y_{j-1} = \frac{Y_j cos(\alpha_j e_j) - i\tilde{n}_j sin(\alpha_j e_j)}{cos(\alpha_j e_j) - i\left(\frac{Y_j}{\tilde{n}_j}\right) sin(\alpha_j e_j)}$$

where the subscript $j$ represents the parameter at layer $j$ and $\alpha_j = \sqrt{\left(\frac{2\pi n_j}{\lambda}\right)^2 - (2\pi\nu)^2}$ with $\nu = n_0 \ sin\theta_0/\lambda$. The equation allows us the calculate the admittance of interface $j-1$, given that the admittance of interface $j$ is known. The admittance at substrate is simply equal to the effective refractive index: $Y_s = \ \tilde{n}_s$.

Having $Y_0$ enables us to find $\nu$ in which $\frac{1}{r(\nu)} = \frac{\tilde{n}_0(\nu) + Y_0(\nu)}{\tilde{n}_0(\nu) - Y_0(\nu)} = 0$. Finally, the effective refractive index can be calculated as $n_e = \nu\lambda$. Notice that the selected wavelengths in the equation are 494 nm for the first sample (Figure 3), 620 nm for the second sample (Figure 5) and the incident polarization is TE.

**Other Characterizations**. Plane views of samples are measured with a FEI Nova nanoSEM 200 scanning electron microscope (SEM) in low vacuum mode with a helix detector. The TEM characterizations are carried out with a Jeol 2021 TEM operated at 200kV and FIB lamellae are prepared with a FIB-FEI Helios 600i instrument.

## AUTHOR CONTRIBUTIONS

The manuscript was written through contributions of the first and last authors.

## CONFLICTS OF INTEREST

There are no conflicts of interest to declare.

## ACKNOWLEDGMENTS

The authors acknowledge Manuel A. Flores Figueroa and Francis Vocanson from Hubert Curien Laboratory for providing the Ag: $TiO_2$ think films on which the experiments have been carried out, and David Troadec from IEMN Laboratory for the preparation of the FIB lamellas. The authors thank Claude Amra and Paul Rouquette for fruitful discussions related to the calculations of guided modes in a multilayer. They also acknowledge the ANR for funding through the project MIXUP (ANR-18-CE39-0010).

## REFERENCES

1 A. Christ, S. G. Tikhodeev, N. A. Gippius, J. Kuhl and H. Giessen, *Phys. Rev. Lett.*, 2003, **91**, 183901.

2 T. Zentgraf, S. Zhang, R. F. Oulton and X. Zhang, *Phys. Rev. B*, 2009, **80**, 195415.

3 V. G. Kravets, A. V. Kabashin, W. L. Barnes and A. N. Grigorenko, *Chem. Rev.*, 2018, **118**, 5912–5951.

4 A. D. Utyushev, V. I. Zakomirnyi and I. L. Rasskazov, *Rev. Phys.*, 2021, **6**, 100051.

5 S. Linden, J. Kuhl and H. Giessen, *Phys. Rev. Lett.*, 2001, **86**, 4688–4691.

6 S. Murai, M. A. Verschuuren, G. Lozano, G. Pirruccio, S. R. K. Rodriguez and J. G. Rivas, *Opt. Express*, 2013, **21**, 4250.

7 G. Quaranta, G. Basset, O. J. F. Martin and B. Gallinet, *Laser. Photonics. Rev.*, 2018, **12**, 1800017.

8 W. Wang, M. Ramezani, A. I. Väkeväinen, P. Törmä, J. G. Rivas and T. W. Odom, *Mater. Today.*, 2018, **21**, 303–314.

9 A. Danilov, G. Tselikov, F. Wu, V. G. Kravets, I. Ozerov, F. Bedu, A. N. Grigorenko and A. V. Kabashin, *Biosens. Bioelectron.*, 2018, **104**, 102–112.

10 X. Zhang, X. Ma, F. Dou, P. Zhao and H. Liu, *Adv. Funct. Mater.*, 2011, **21**, 4219–4227.

11 S. Sarkar, V. Gupta, M. Kumar, J. Schubert, P. T. Probst, J. Joseph and T. A. F. König, *ACS Appl. Mater. Interfaces*, 2019, **11**, 13752–13760.

12 S. V. Zhukovsky, V. E. Babicheva, A. V. Uskov, I. E. Protsenko and A. V. Lavrinenko, *Plasmonics*, 2014, **9**, 283–289.

13 W. H. Koo, W. Youn, P. Zhu, X.-H. Li, N. Tansu and F. So, *Adv. Funct. Mater.*, 2012, **22**, 3454–3459.

14 G. Lozano, G. Grzela, M. A. Verschuuren, M. Ramezani and J. G. Rivas, *Nanoscale*, 2014, **6**, 9223–9229.

15 G. Si, Y. Zhao, J. Lv, M. Lu, F. Wang, H. Liu, N. Xiang, T. J. Huang, A. J. Danner, J. Teng and Y. J. Liu, *Nanoscale*, 2013, **5**, 6243.

16 H. Wang, X. Wang, C. Yan, H. Zhao, J. Zhang, C. Santschi and O. J. F. Martin, *ACS Nano*, 2017, **11**, 4419–4427.

17 Y. Gu, L. Zhang, J. K. W. Yang, S. P. Yeo and C.-W. Qiu, *Nanoscale*, 2015, **7**, 6409–6419.

18 I. Koirala, V. R. Shrestha, C.-S. Park, S.-S. Lee and D.-Y. Choi, *Sci. Rep.*, 2017, **7**, 40073.

19 D. Khlopin, F. Laux, W. P. Wardley, J. Martin, G. A. Wurtz, J. Plain, N. Bonod, A. V. Zayats, W. Dickson and D. Gérard, *J. Opt. Soc. Am. B*, 2017, **34**, 691.

20 X. Zhu, W. Yan, U. Levy, N. A. Mortensen and A. Kristensen, *Sci. Adv.*, 2017, **3**, e1602487.

21 X. Zhu, J. Engelberg, S. Remennik, B. Zhou, J. N. Pedersen, P. Uhd Jepsen, U. Levy and A. Kristensen, *Nano Lett.*, 2022, **22**, 2786–2792.

22 M. Juodėnas, T. Tamulevičius, J. Henzie, D. Erts and S. Tamulevičius, *ACS Nano*, 2019, **13**, 9038–9047.

23 K. Volk, J. P. S. Fitzgerald, P. Ruckdeschel, M. Retsch, T. A. F. König and M. Karg, *Adv. Opt. Mater.*, 2017, **5**, 1600971.

24 M. B. Ross, J. C. Ku, M. G. Blaber, C. A. Mirkin and G. C. Schatz, *Proc. Natl. Acad. Sci. U.S.A.*, 2015, **112**, 10292–10297.

25 M. Mayer, M. J. Schnepf, T. A. F. König and A. Fery, *Adv. Opt. Mater.*, 2019, **7**, 1800564.

26 V. Gupta, P. T. Probst, F. R. Goßler, A. M. Steiner, J. Schubert, Y. Brasse, T. A. F. König and A. Fery, *ACS Appl. Mater. Interfaces*, 2019, 8.

27 N. Dalloz, V. D. Le, M. Hebert, B. Eles, M. A. Flores Figueroa, C. Hubert, H. Ma, N. Sharma, F. Vocanson, S. Ayala and N. Destouches, *Adv. Mater.*, 2022, **34**, 2104054.

28 N. Destouches, N. Sharma, M. Vangheluwe, N. Dalloz, F. Vocanson, M. Bugnet, M. Hébert and J. Siegel, *Adv. Funct. Mater.*, 2021, **31**, 2010430.

29 N. Destouches, N. Crespo-Monteiro, G. Vitrant, Y. Lefkir, S. Reynaud, T. Epicier, Y. Liu, F. Vocanson and F. Pigeon, *J. Mater. Chem. C*, 2014, **2**, 6256–6263.

30 Z. Liu, J. Siegel, M. Garcia-Lechuga, T. Epicier, Y. Lefkir, S. Reynaud, M. Bugnet, F. Vocanson, J. Solis, G. Vitrant and N. Destouches, *ACS Nano*, 2017, **11**, 5031–5040.

31 N. Sharma, N. Destouches, C. Florian, R. Serna and J. Siegel, *Nanoscale*, 2019, **11**, 18779–18789.

32 B. Eles, P. Rouquette, J. Siegel, C. Amra, J. Lumeau, A. Moreau, C. Hubert, M. Zerrad and N. Destouches, *Nanophotonics*, 2022, **11**, 2303–2318.

33 S. R. K. Rodriguez, Y. T. Chen, T. P. Steinbusch, M. A. Verschuuren, A. F. Koenderink and J. G. Rivas, *Phys. Rev. B*, 2014, **90**, 235406.

34 N. Destouches, J. Martínez-García, M. Hébert, N. Crespo-Monteiro, G. Vitrant, Z. Liu, A. Trémeau, F. Vocanson, F. Pigeon, S. Reynaud and Y. Lefkir, *J. Opt. Soc. Am. B*, 2014, **31**, C1.

35 Z. Liu, T. Epicier, Y. Lefkir, G. Vitrant and N. Destouches, *J. Microsc.*, 2017, **266**, 60–68.

36 H. Ma, S. Bakhti, A. Rudenko, F. Vocanson, D. S. Slaughter, N. Destouches and T. E. Itina, *J. Phys. Chem. C*, 2019, **123**, 25898–25907.

37 Z. Liu, G. Vitrant, Y. Lefkir, S. Bakhti and N. Destouches, *Phys. Chem. Chem. Phys.*, 2016, **18**, 24600–24609.

38 Z. Liu, N. Destouches, G. Vitrant, Y. Lefkir, T. Epicier, F. Vocanson, S. Bakhti, Y. Fang, B. Bandyopadhyay and M. Ahmed, *J. Phys. Chem. C*, 2015, **119**, 9496–9505.

39 A. Wokaun, J. P. Gordon and P. F. Liao, *Phys. Rev. Lett.*, 1982, **48**, 957–960.

40 U. Kreibig and M. Vollmer, *Optical Properties of Metal Clusters*, Springer Berlin Heidelberg, Berlin, Heidelberg, 1995, vol. 25.

41 S. Bakhti, N. Destouches and A. V. Tishchenko, *Journal of Quantitative Spectroscopy and Radiative Transfer*, 2014, **146**, 113–122.

42 S. R. K. Rodriguez, S. Murai, M. A. Verschuuren and J. G. Rivas, *Phys. Rev. Lett.*, 2012, **109**, 166803.

43 C. Amra, M. Lequime and M. Zerrad, *Electromagnetic Optics of Thin-Film Coatings: Light Scattering, Giant Field Enhancement, and Planar Microcavities*, Cambridge University Press, 1st edn., 2020.

44 A. Egel, K. M. Czajkowski, D. Theobald, K. Ladutenko, A. S. Kuznetsov and L. Pattelli, *J. Quant. Spectrosc. Radiat. Transf.*, 2021, **273**, 107846.

45 A. Egel and U. Lemmer, *J. Quant. Spectrosc. Radiat. Transf.*, 2014, **148**, 165–176.

46 A. Egel, Accurate Optical Simulation of Disordered Scattering Layers for Light Extraction from Organic Light Emitting Diodes. Doctoral dissertation, Karlsruhe Institute of Technology (KIT), 2018.